Journal of Sound and Vibration (2001) **243**(4), 659–678
doi:10.1006/jsvi.2000.3435, available online at http://www.idealibrary.com on IDEAL®

ACOUSTIC ABSORPTION OF MACRO-PERFORATED POROUS MATERIALS

N. ATALLA AND R. PANNETON

Groupe d'Acoustique de l'Université de Sherbrooke, Department of Mechanical Engineering, Univ. de Sherbrooke, Sherbrooke, QC, J1K2R1, Canada

AND

F. C. SGARD AND X. OLNY

Laboratoire des Sciences de l'Habitat, DGCB URA CNRS 1652, *Ecole Nationale des Travaux Publics de l'Etat*, 69518 *Vaulx-en-Velin Cedex, France. E-mail: franck.sgard@entpe.fr*

(*Received* 2 *February* 2000, *and in final form* 8 *August* 2000)

The paper discusses the absorption of non-homogeneous thin macro-porous materials. In particular, the acoustic absorption performance of three-dimensional (3-D) porous media made up from thin porous patches, with different acoustic properties, is investigated using a numerical model. The presented model considers the configuration wherein the material is bonded onto the hard-walled termination of a semi-infinite rectangular waveguide. It couples a finite element description for the porous material to a modal description in the waveguide and uses a power balance approach to accurately quantify the absorption performance of the material. Experimental results are presented to validate the model in the special case of a macro-perforated porous material. Using this model a parameter study is presented. It is shown that absorption may be increased at low frequency by using non-homogeneous patch-works.

1. INTRODUCTION

The acoustic absorption performance of porous materials is poor at low frequencies. For a given thickness, this performance may be improved by using stratified media [1] and/or special configurations such as membrane resonators. For simple stratified media, analytical methods (e.g. transfer matrix method: TMM) may be used to evaluate the acoustical properties in the context of the Biot theory [1–3]. For thin layers at low frequencies the Biot theory can be replaced by simpler models where the porous frame is motionless [4], and the air in the porous medium is replaced by an equivalent complex fluid. Nevertheless, these formulations are limited to one-dimensional (1-D) propagation and cannot be used to investigate more complex 3-D configurations that may present *a priori* improved performances. The recent venue of finite element based numerical formulations [5–7] for porous materials opens the way for the modelling of such configurations.

Atalla *et al.* [8] compared an approximate general method of predicting the surface impedance at low frequencies for non-homogeneous thin porous layers, based on a non-propagative representation of the acoustic field in the layer, to a finite element based method, for different three-dimensional porous patchworks. They found comparable results and concluded that propagative phenomena in sound absorption for non-homogeneous

0022-460X/01/240659 + 20 $35.00/0

thin porous layers are not important. However, their theoretical model was approximate and neglected in particular the possible interaction between the different patches. In the present paper, a more accurate model is presented and validated experimentally. It consists of a non-homogeneous porous material, made up from thin porous patches, bonded onto the hard termination of a infinite rectangular waveguide. Each thin patch is assumed to behave as an equivalent fluid, that is, the frames of the porous media are assumed motionless. The coupling between the porous material and the waveguide is accounted for explicitly using the modal behavior of the waveguide. Using a power balance approach the performance of the porous material is investigated in terms of its absorption coefficient and acoustic powers dissipated by thermal and viscous mechanisms. Using this model, the absorption performance of media with double porosity is studied.

Acoustics of media with double porosity was first studied by Auriault *et al.* [9]. Using the periodic structures homogenization method (HSP) applied to multiscales materials, they showed that the macroscopic behavior highly depends on the interscale ratio of characteristic sizes identified in the materials. In the case of rigid porous materials, Boutin *et al.* [10] identified a case of particular interest which exhibits a partial coupling between the pores and the micro-pores: the pressure in the micro-porous domain is not uniform and the pressure difference in the pores and in the micro-pores satisfies a diffusion equation, at the first order of approximation. The problem raises a characteristic frequency separating the total coupling frequency domain (low frequencies) and the no-coupling frequency domain (high frequencies). This characteristic frequency is related to the mesoscopic geometry and to the porosity and the static flow resistance of the micro-porous media. A more general description, obtained via the HSP method, has been recently proposed in order to clarify the possible behaviors of double-porosity media [11, 12]. It appears that the macroscopic behavior is highly dependent on the permeabilities contrast between the macro-pores and the micro-pores. Agreement between proposed models and experimental results are very good in the case of perforated porous panels. They also showed that the absorption coefficient could be increased in a given frequency band by fixing the diffusion frequency properly. However, this model is currently limited to air-filled macro-pores and laterally infinite materials. The proposed model goes beyond these two limitations. It is used in the present paper to investigate the effects of macro-porosity, distribution and nature of the macro-pores on acoustic absorption.

The organization of the rest of the paper is as follows. Firstly, the finite element formulation of the problem is presented together with a detailed discussion of the calculation of different acoustic indicators that will help explain the governing absorption mechanisms. Secondly, experimental results are presented to validate the soundness of the model in the special case of a macro-perforated porous material. Finally, a numerical parameter study is presented to illustrate the absorption mechanisms and performance for different three-dimensional macro-porous materials.

2. THEORY

2.1. DESCRIPTION OF THE PROBLEM

The geometry of the problem is depicted in Figure 1. It consists of a three-dimensional patchwork inserted in a semi-infinite rectangular waveguide. The system is excited by an incoming plane wave propagating in the waveguide. Each 3-D patch is rectangular and is made from a homogeneous porous material modelled as an equivalent fluid. The density and sound speed in the waveguide are denoted by ρ_0 and c_0 respectively. In the following, a temporal dependency $e^{j\omega t}$ for all the fields is assumed.

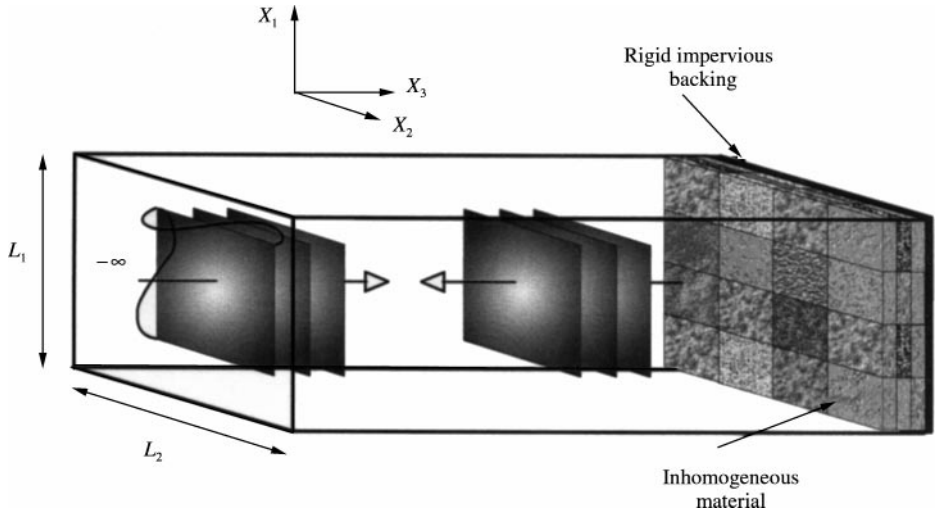

Figure 1. Geometry of the problem.

2.2. THE EQUIVALENT FLUID MODEL

As mentioned in the introduction, for thin layers at low frequencies, the porous frame may be assumed motionless. In this case, the porous material is equivalent to a fluid. Its acoustical properties are completely defined with a set of two acoustical characteristics, for instance, $\tilde{\rho}_{22}$ and $\tilde{R}$ where $\tilde{\rho}_{22}$ is the modified Biot's density of the fluid phase accounting for viscous dissipation and $\tilde{R}$ may be interpreted as the bulk modulus of the air occupying a fraction ϕ of a unit volume aggregate [1]. The equation of propagation in an equivalent fluid is given by [1, 3]

$$\Delta p + \omega^2 \frac{\tilde{\rho}_{22}}{\tilde{R}} p = 0, \tag{1}$$

where p is the pressure in the equivalent fluid.

The associated weak integral form is given by

$$\int_{\Omega^p} \left[\frac{\phi^2}{\omega^2 \tilde{\rho}_{22}} \nabla p \cdot \nabla \delta p - \frac{\phi^2}{\tilde{R}} p \delta p \right] \mathrm{d}\Omega - \int_{\partial\Omega^p} \frac{\phi^2}{\omega^2 \tilde{\rho}_{22}} \frac{\partial p}{\partial n} \delta p \, \mathrm{d}S = 0 \quad \forall \delta p, \tag{2}$$

where δp is an arbitrary admissible variation of p. $\partial p/\partial n$ is the normal derivative of p with respect to the unit normal vector $\mathbf{n}$ external to the bounding surface $\partial\Omega^p$ enclosing the porous material volume Ω^p. The volume integral represents the sum of the work, developed in the virtual displacement field associated with δp, by internal and inertia forces in the porous medium. Given the chosen boundary conditions, the surface integral in equation (2) is only non-zero on the porous-air interface. The surface integral represents the virtual work done by the internal pressure at the boundary of the acoustic domain due to an imposed motion on its surface.

2.3. WAVEGUIDE MODELLING

Let p^a denote the acoustic pressure in the waveguide represented in Figure 1. At the porous–air interface ($x_3 = 0$), the pressure and normal displacement are continuous:

$$\begin{aligned} p &= p^a, \\ u_n^a &= \frac{1}{\rho_0 \omega^2} \frac{\partial p^a}{\partial n} = \frac{\phi^2}{\tilde{\rho}_{22} \omega^2} \frac{\partial p}{\partial n}. \end{aligned} \tag{3}$$

Thus, the boundary term in equation (2) takes the form

$$\int_{\partial\Omega^p} \frac{\phi^2}{\omega^2 \tilde{\rho}_{22}} \frac{\partial p}{\partial n}\, \delta p \, \mathrm{d}S = \int_{\partial\Omega^p} \frac{1}{\omega^2 \rho_0} \frac{\partial p^a}{\partial n}\, \delta p \, \mathrm{d}S \tag{4}$$

To calculate $u_n^a = (1/\rho_0\omega^2)\, \partial p^a/\partial n$, the pressure p^a is written as the sum of the blocked pressure p_b satisfying $\partial p_b/\partial n|_{\partial\Omega_p} = 0$ and the pressure p_{rad} radiated from the surface of the patch-work media:

$$p^a = p_b + p_{rad}. \tag{5}$$

For a normal mode excitation of amplitude p_0, p_b reduces to $2p_0$. The radiated pressure may be expressed in terms of the orthogonal normal modes φ_{mn} in the waveguide:

$$p_{rad}(\mathbf{x}) = \sum_{m,n} B_{mn} \varphi_{mn}(x_1, x_2)\, \mathrm{e}^{\mathrm{j}k_{mn}x_3}, \tag{6}$$

where $\mathbf{x} = (x_1, x_2, x_3)$, $k_{mn}^2 = k^2 - (m\pi/L_1)^2 - (n\pi/L_2)^2$ for a waveguide with a rectangular cross-section $(L_1 \times L_2)$ and B_{mn} are modal amplitudes obtained from the mode orthogonality properties:

$$\int_{\partial\Omega^p} p_{rad}\, \varphi_{mn}(x_1, x_2)\, \mathrm{d}S_x = \int_{\partial\Omega^p} (p^a - p_b) \varphi_{mn}(x_1, x_2)\, \mathrm{d}S_x \tag{7}$$

which leads to

$$B_{mn} = \frac{1}{N_{mn}} \int_{\partial\Omega^p} (p - p_b)\, \varphi_{mn}(x_1, x_2)\, \mathrm{d}S_x, \tag{8}$$

where

$$N_{mn} = \int_{\partial\Omega^p} |\varphi_{mn}(x_1, x_2)|^2\, \mathrm{d}S_x \tag{9}$$

is the norm of mode (m, n).

Using equations (6) and (9) the normal displacement at the patch-work–air interface, $x_3 = 0$ can be written in the form

$$u_n^a(\mathbf{x}) = \frac{1}{\mathrm{j}\omega} \int_{\partial\Omega^p} \boldsymbol{A}(\mathbf{x}, \mathbf{y})\, (p(\mathbf{y}) - p_b(\mathbf{y})\, \mathrm{d}S_y, \tag{10}$$

where $\boldsymbol{A}$ is the following admittance operator:

$$\boldsymbol{A}(\mathbf{x}, \mathbf{y}) = \sum_{mn} \frac{k_{mn}}{\rho_0 \omega N_{mn}}\, \varphi_{mn}(\mathbf{x}) \varphi_{mn}(\mathbf{y}) \tag{11}$$

Substituting expression (10) for $u_n^a = (1/\rho_0\omega^2)(\partial p^a/\partial n)$ in equation (4) leads to the following expression for the boundary coupling term:

$$\begin{aligned} \int_{\partial\Omega^p} \frac{\phi^2}{\omega^2 \tilde{\rho}_{22}} \frac{\partial p}{\partial n}\, \delta p \, \mathrm{d}S = {} & \frac{1}{\mathrm{j}\omega} \int_{\partial\Omega^p} \int_{\partial\Omega^p} \boldsymbol{A}(\mathbf{x}, \mathbf{y}) p(\mathbf{y}) \delta p(\mathbf{x})\, \mathrm{d}S_y\, \mathrm{d}S_x \\ & - \frac{1}{\mathrm{j}\omega} \int_{\partial\Omega^p} \int_{\partial\Omega^p} \boldsymbol{A}(\mathbf{x}, \mathbf{y}) p_b(\mathbf{y}) \delta p(\mathbf{x})\, \mathrm{d}S_y\, \mathrm{d}S_x \end{aligned} \tag{12}$$

This form has the advantage of depicting the coupling with the waveguide in terms of radiation admittance and blocked-pressure loading. Note that at low frequencies (below the cut-off frequency of the waveguide), higher modes lead to a purely imaginary admittance operator of an inertance type.

Finally, the weak integral form of the equations governing the porous layer coupled with the modal behavior of the waveguide is obtained from equations (2) and (12):

$$\int_{\Omega^p}\left[\frac{\phi^2}{\omega^2\tilde{\rho}_{22}}\nabla p\cdot\nabla\delta p-\frac{\phi^2}{\tilde{R}}p\delta p\right]\mathrm{d}\Omega-\frac{1}{\mathrm{j}\omega}\int_{\partial\Omega^p}\int_{\partial\Omega^p}\boldsymbol{A}(\mathbf{x},\mathbf{y})p(\mathbf{y})\delta p(\mathbf{x})\,\mathrm{d}S_y\,\mathrm{d}S_x$$
$$+\frac{1}{\mathrm{j}\omega}\int_{\partial\Omega^p}\int_{\partial\Omega^p}\boldsymbol{A}(\mathbf{x},\mathbf{y})p_b(\mathbf{y})\delta p(\mathbf{x})\,\mathrm{d}S_y\,\mathrm{d}S_x=0\quad\forall\delta p. \tag{13}$$

For a given number of normal modes kept φ_{mn} in the waveguide, equation (13) is discretized using the finite element method and solved for the pressure variable in the porous medium.

2.4. DISSIPATED POWERS IN THE POROUS MEDIA

In this section, expressions for the powers dissipated through the different mechanisms governing dissipation in the porous–rigid media are derived. Following the classical steps leading to the weak integral form equation (2) with the following particular choice for the admissible function: $-\mathrm{j}\omega p^*$, one obtains

$$\underbrace{\mathrm{j}\omega\int_{\Omega^p}\frac{\phi^2}{\tilde{R}}p\,p^*\mathrm{d}\Omega}_{\Pi_{int}}\ \underbrace{-\mathrm{j}\omega\int_{\Omega^p}\frac{\phi^2}{\omega^2\tilde{\rho}_{22}}\nabla\mathrm{p}\cdot\nabla p^*\mathrm{d}\Omega}_{\Pi_{iner}}\ \underbrace{+\int_{\partial\Omega^p}\mathrm{j}\omega\,u_n^a(\mathbf{x})p^*(\mathbf{x})\,\mathrm{d}S}_{-\Pi_{trans}}=0. \tag{14}$$

This provides the following power balance equation:

$$\Pi_{int}+\Pi_{iner}-\Pi_{trans}=0, \tag{15}$$

where Π_{int}, Π_{iner} represent the power developed by the internal and inertia forces in the interstitial fluid, respectively and Π_{trans} represents the power flowing into the waveguide–porous interface. Π_{trans} can be written in turn in terms of incident and reflected powers.

The time-averaged power dissipated within the system is given by

$$\Pi_{diss}=\frac{1}{2}\Re\left[\int_{\partial\Omega^p}\mathrm{j}\omega u_n^a(\mathbf{x})p^*(\mathbf{x})\,\mathrm{d}S\right]. \tag{16}$$

It can be subdivided into contributions from powers dissipated through viscous and thermal effects: $\Pi_{diss}=\Pi_{diss}^v+\Pi_{diss}^t$. The time-averaged power dissipated through viscous effects is obtained from, Π_{iner}, namely

$$\Pi_{diss}^v=\frac{1}{2}\Im\left[\int_{\Omega^p}\frac{\phi^2}{\omega\tilde{\rho}_{22}}\nabla p\cdot\nabla p^*\,\mathrm{d}\Omega\right]. \tag{17}$$

The power dissipated through thermal effects is obtained from, Π_{int}, namely

$$\Pi_{diss}^t=-\frac{1}{2}\Im\left[\omega\int_{\Omega^p}\frac{\phi^2}{\tilde{R}}p\,p^*\,\mathrm{d}\Omega\right]. \tag{18}$$

2.5. ABSORPTION COEFFICIENT

To characterize the absorption performance of the 3-D studied patch-works, one defines its power absorption coefficient:

$$\alpha = \Pi_{diss}/\Pi_{inc} = (\Pi^{v}_{diss} + \Pi^{t}_{diss})/\Pi_{inc}, \tag{19}$$

where Π_{inc} is the incident power. In the case of a plane wave excitation, of amplitude p_0, the incident power is given by

$$\Pi_{inc} = S|p_0|^2/2\rho_0 c_0, \tag{20}$$

where S is the cross-section of the waveguide. Note that at low frequencies (i.e. below the cut-off frequency of the waveguide), only the (0, 0) order mode contribute to the real part of the admittance and a simplified expression for the dissipated power can be obtained using equations (10) and (11):

$$\Pi_{diss} = \Pi_{inc} - \Pi_{ref}, \tag{21}$$

where Π_{ref} is the reflected power given by

$$\Pi_{ref} = S|p_{avg} - p_0|^2/2\rho_0 c_0 \tag{22}$$

and p_{avg} is the surface-averaged pressure.

Strictly speaking, for a non-homogeneous patch work a surface impedance is meaningless: the patch-work cannot be considered locally reacting; there is a transverse variation of the pressure and the normal velocity at the surface of the patch-work. This means in turn that keeping only the propagating plane wave mode (0, 0) is not sufficient to correctly solve the problem; higher evanescent modes must be accounted for in equation (6). However, in a Kundt tube, an average impedance can be measured by standard methods. As a consequence, one can also define a space-averaged surface impedance at a distance d down the waveguide by

$$Z_d = \int_S p^a(x_1, x_2, -\mathrm{d})\,\mathrm{d}S \Big/ \mathrm{j}\omega \int_S u^a_n(x_1, x_2, -\mathrm{d})\,\mathrm{d}S\,. \tag{23}$$

The pressure and the normal velocity are calculated from equations (3, 5, 6) and (8) at a distance d from the material surface. The surface impedance, Z_s is next calculated using the classical plane wave relationship:

$$Z_S = \frac{Z_d \cos(kd) + \mathrm{j}Z_0 \sin(kd)}{Z_0 \cos(kd) + \mathrm{j}Z_d \sin(kd)} \tag{24}$$

with $Z_0 = \rho_0 c_0$.

3. EXPERIMENTAL VALIDATION

The presented method has been validated first by considering homogeneous porous media. Next, an experimental validation has been performed in the case of a double-porosity material. The tested sample consists of a mineral wool with periodic

cylindrical holes (referred to as macro-pores). Such a material is denoted as having *double porosity*. Figure 2 represents a simplified schematic of the tested sample. In this figure, the macro-pores are depicted to have a square cross-section. This simplification has been used to simplify the meshing process required for the numerical simulations of the experiment. It is seen in Figure 2 that the tested sample consists of a periodic lattice made up of several periods of a generic cell. The generic cell consists of a square ($L_c \times L_c$) mineral wool sample from which a center square hole with dimension ($a \times a$) has been cut out. The porosity of the wool and the porosity associated with the holes will be denoted by micro-porosity ϕ_m and macro-porosity ϕ_p respectively. The macro-porosity ϕ_p corresponding to the configuration of interest is given by

$$\phi_p = a^2/L_c^2 \,. \tag{25}$$

The tested sample is made from 1 generic cell: $L_c = 0{\cdot}085$ m and a cylindrical macro-pore of radius equal to 0·016 m. The acoustic properties of the material are given in Table 1. Measurements have been performed using a Kundt tube of (0·085 m × 0·085 m) square section ($L_1 = L_2 = L = L_c$). A single microphone transfer function method has been employed to determine normal acoustic surface impedances of the samples excited with a sinusoidal pseudorandom noise signal. For the numerical simulations, first note that in the case of normal incidence, because of symmetry it is possible to reduce the study of the arrangement depicted in Figure 2 to one cell. Indeed at the boundary between two cells, the velocity components perpendicular to the boundary are equal to zero. The pressure field at the cell's face is given by

$$p(x_1, x_2, 0) = \sum_{m,n} C_{mn} \cos\left(\frac{2\pi m}{L_c} x_1\right) \cos\left(\frac{2\pi n}{L_c} x_2\right) \tag{26}$$

since in this special symmetric case, modes with odd indices are not excited. Consequently, the presented numerical results have been obtained by modelling one generic cell.

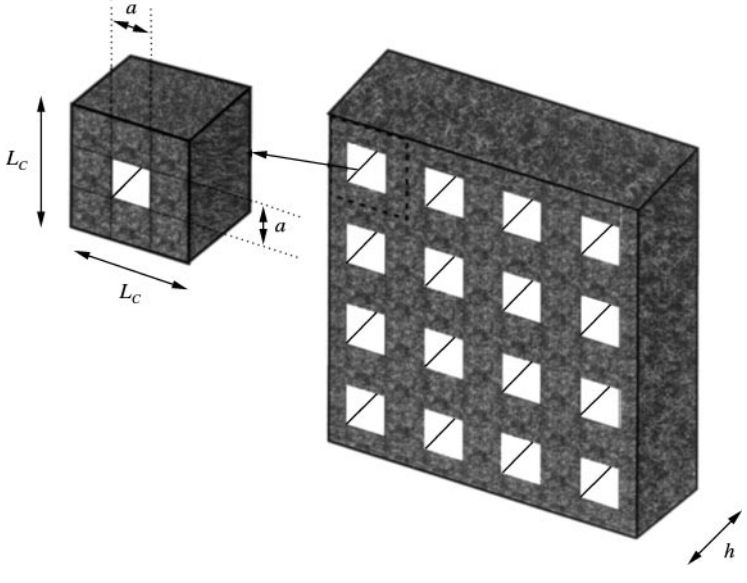

Figure 2. Double-porosity material.

TABLE 1

Physical properties and dimensions

Material 1: *Rock-wool*	
Flow resistivity	$\sigma_m = 135\,000\,\mathrm{N\,m^{-4}\,s}$
Porosity	$\phi_m = 0{\cdot}94$
Tortuosity	$\alpha_\infty = 2{\cdot}1$
Viscous characteristic length	$\Lambda = 49 \times 10^{-6}\,\mathrm{m}$
Thermal characteristic length	$\Lambda' = 166 \times 10^{-6}\,\mathrm{m}$
Poisson's ratio	$\nu = 0$
In vacuo Young's modulus	$E = 4400\,000\,\mathrm{Pa}$
Loss factor	$\eta = 0{\cdot}1$
Solid-phase mass density	$\rho_s = 2167\,\mathrm{kg/m^3}$
Material 2: *Rigid glass-wool* (*RGW*)	
Flow resistivity	$\sigma_m = 9000\,\mathrm{N\,m^{-4}\,s}$
Porosity	$\phi_m = 0{\cdot}99$
Turtuosity	$\alpha_\infty = 1$
Viscous characteristic length	$\Lambda = 192 \times 10^{-6}\,\mathrm{m}$
Thermal characteristic length	$\Lambda' = 384 \times 10^{-6}\,\mathrm{m}$
Poisson's ratio	$\nu = 0$
In vacuo Young's modulus	$E = 440\,000\,\mathrm{Pa}$
Loss factor	$\eta = 0{\cdot}1$
Solid-phase mass density	$\rho_s = 1630\,\mathrm{kg/m^3}$

The dimension of the hole cross-section has been adjusted to $a = 0{\cdot}0283\,\mathrm{m}$ to conserve the macro-porosity of the tested sample. Finally, the number of kept modes and the corresponding lateral mesh have been checked for convergence.

Figure 3 shows the comparison between simulation and measurements for two thicknesses: (a) 5·75 and (b) 11·5 cm. Excellent agreement is found, validating the proposed method. To re-emphasize the importance of evanescent modes, Figure 4 shows the number of kept (evanescent) modes necessary to reach convergence in the case of 11·5 cm thick material. Figure 5 presents the comparison of the surface impedance between prediction using equation (23) and measurements for a 11·5 cm thick double-porosity material ($\phi_p = 0{\cdot}11$). The comparison is acceptable keeping in mind that because of the variation of the pressure in the transverse direction, only an averaged surface impedance is calculated. This calculation is acceptable when a global indicator such as the absorption coefficient is needed. Indeed, the absorption coefficient calculated from the averaged surface impedance and the power balance are the same. However, the interpretation of the averaged surface impedance must be handled with care. The authors believe that in such cases of non-homogeneous materials only the global absorption coefficient and the dissipated powers calculated from the power balance of the system are meaningful. These are the indicators that will be used in the following numerical results.

4. NUMERICAL RESULTS

As mentioned in the Introduction, for a double-porosity material, the pressure in the micro-porous domain is not uniform and the pressure difference in the pores and in the micro-pores satisfies a diffusion equation. The absorption performance of such materials is linked to a characteristic frequency referred to as the diffusion frequency. The diffusion frequency for a double porosity material is given by [12]

$$\omega_d = 8P_0/\sigma_m \phi_m M_d \Lambda_d^2, \tag{27}$$

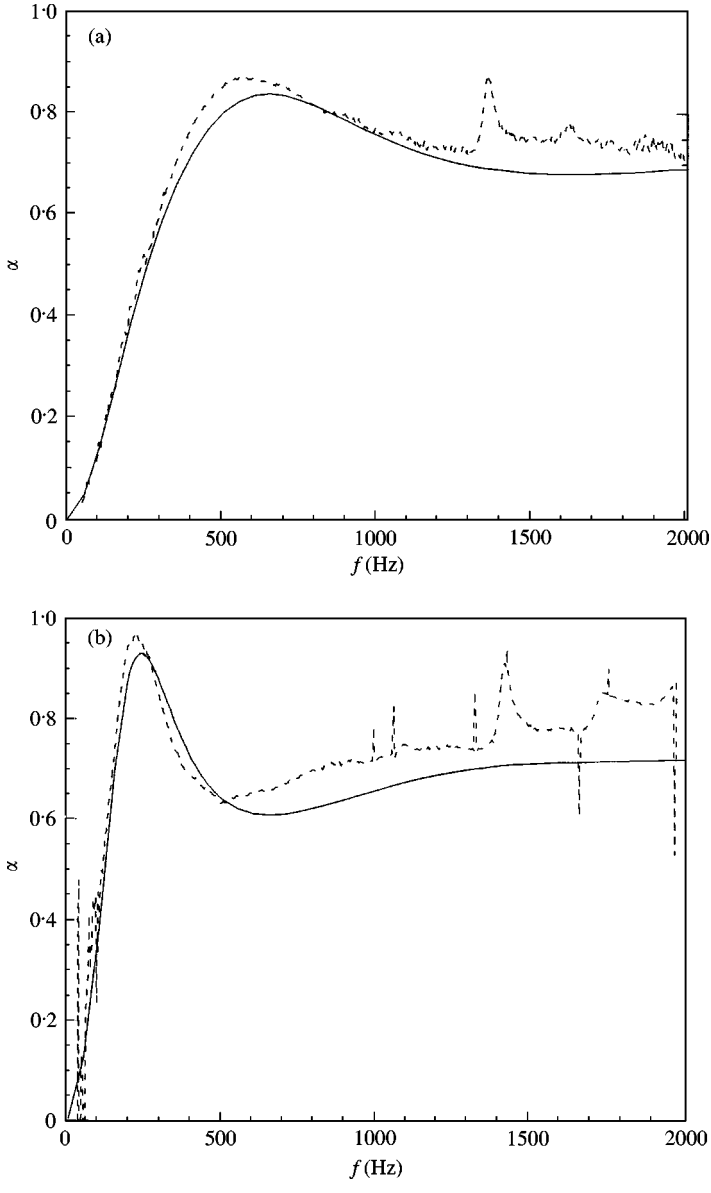

Figure 3. Comparison between prediction and measurements for a double-porosity rock-wool: (a) 5·75 cm thick; (b) 11·5 cm thick: ——, simulation; — — —, measurement.

where σ_m is the flow resistivity of the porous material, $P_0 = 101300$ Pa, M_d is a shape factor which depends on the hole shapes and on the macro-pores distribution. This coefficient has been introduced by Olny [12] and reads:

$$M_d = 8D_{eq}/\Lambda_d^2(1 - \phi_p), \tag{28}$$

D_{eq} is a function which depends on the geometry of the hole lattices, Λ_d is a characteristic length associated to the diffusion process. It is related to the ratio of the volume and the surface of the macro-pores in contact with the porous material. For a square hole with size

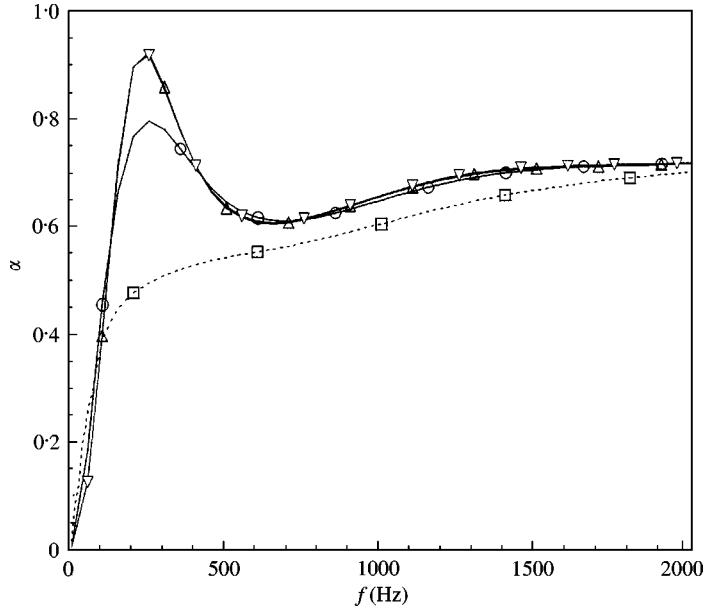

Figure 4. Effects of evanescent modes on the absorption coefficient. –□–, (m, n) = (0, 0); —○—, (m, n) = (2, 2); —△—, (m, n) = (4, 4); —▽—, (m, n) = (6, 6).

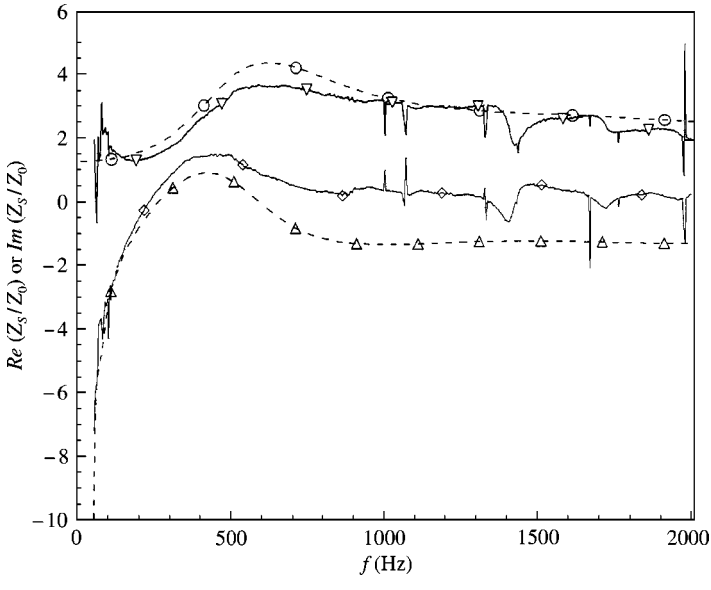

Figure 5. Comparison of the measured and predicted average surface impedance —○— —, simulation: real part; —△— —, simulation: imaginary part; —▽—, measurement: real part; —◇—, measurement: imaginary part.

a in a porous cell of size L_c and thickness h, Λ_d is given by

$$\Lambda_d = \frac{(L_c^2 - a^2)h}{(4ah + (L_c^2 - a^2))} = \frac{(1 - \phi_p)}{((1 - \phi_p)/h + 4\phi_p/a)}. \tag{29}$$

Note that M_d can only be calculated analytically for porous materials with infinite thickness and simple geometry hole lattices [12]. For finite thicknesses, M_d can only be determined experimentally from the knowledge of Λ_d and ω_d. ω_d is found by fitting the analytical impedance model to experimental data.

For double-porosity materials, it is seen that the acoustic behavior of the whole material is governed by three important parameters: the size of the hole, the macro-porosity and a shape factor. Using the proposed model, the next sections are devoted to a numerical study of the influence of these parameters on the absorption coefficient and the powers dissipated in a macro-porous material. In particular the following cases are investigated: (1) the effect of the macro-porosity keeping the hole size constant; (2) the effect of the hole size keeping the macro-porosity constant; (3) the effect of the shape factor for constant macro-porosity and cell sizes; (4) the effect of the flow resistivity of the micro-porous material; and (5) the effect of the nature of the material in the macro-pores. Finally, a comparison between a classical double-layer material and an equivalent heterogeneous material is presented. In the following, all numerical simulations are performed on a 11·5 cm thick rock-wool whose characteristics are specified in Table 1.

4.1. INFLUENCE OF THE MACRO-POROSITY

Figure 6 presents one section of the configuration of interest. The size of the hole (in light grey in the figure) is kept constant equal to 2·83 cm while the macro-porosity is increased from 0·04 to 0·51. Figure 7 shows the evolution of the absorption coefficient as the macro-porosity is increased. For porosities larger than 0·04, it is seen that a slight loss of absorption first occurs at very low frequencies followed by an important gain over the rest of the spectrum. At high frequencies the absorption of all the materials become comparable (not shown on the figure). For double-porosity material, a first peak occur in the frequency range 250–500 Hz according to the value of the macro-porosity. The higher the macro-porosity, the higher the frequency of this peak. This peak increases as the value of macro-porosity increases from 0·04 to 0·18, but tends to be damped for higher values of macro-porosity, until it disappears for large macro-porosities ($\phi_p \geqslant 0{\cdot}51$). However, for high macro-porosity, a second peak appears at frequencies higher than 1000 Hz. It is therefore seen that the macro-porosity can be chosen in order to achieve a maximum absorption in a given frequency range. At low frequencies, a small macro-porosity gives better results whereas a higher macro-porosity allows to control the absorption at high frequencies. Figure 8 shows the contribution of the thermal and viscous dissipation mechanisms, respectively, to the absorption coefficient for each case described in Figure 6. It is clearly seen that both thermal and viscous dissipation increase in the non-homogeneous configuration; the strongest contribution is due to the viscous dissipation.

4.2. INFLUENCE OF THE HOLE SIZE

Figure 9 describes one section of the configuration of interest. The macro-porosity is kept constant equal to 0·11 while the size of the hole (in light grey in the figure) is varied from $a/4$ to $2a$ where $a = 2{\cdot}83$ cm. Figure 10 presents the corresponding absorption coefficients. It is seen that for all hole sizes, the absorption coefficient has a distinct peak at low frequencies. The frequency position and the bandwidth of this peak increase with the hole size. For small hole sizes, the absorption coefficient has a second distinct peak. The height of the first peak increases with the hole size while the inverse is observed for the secondary peak. The

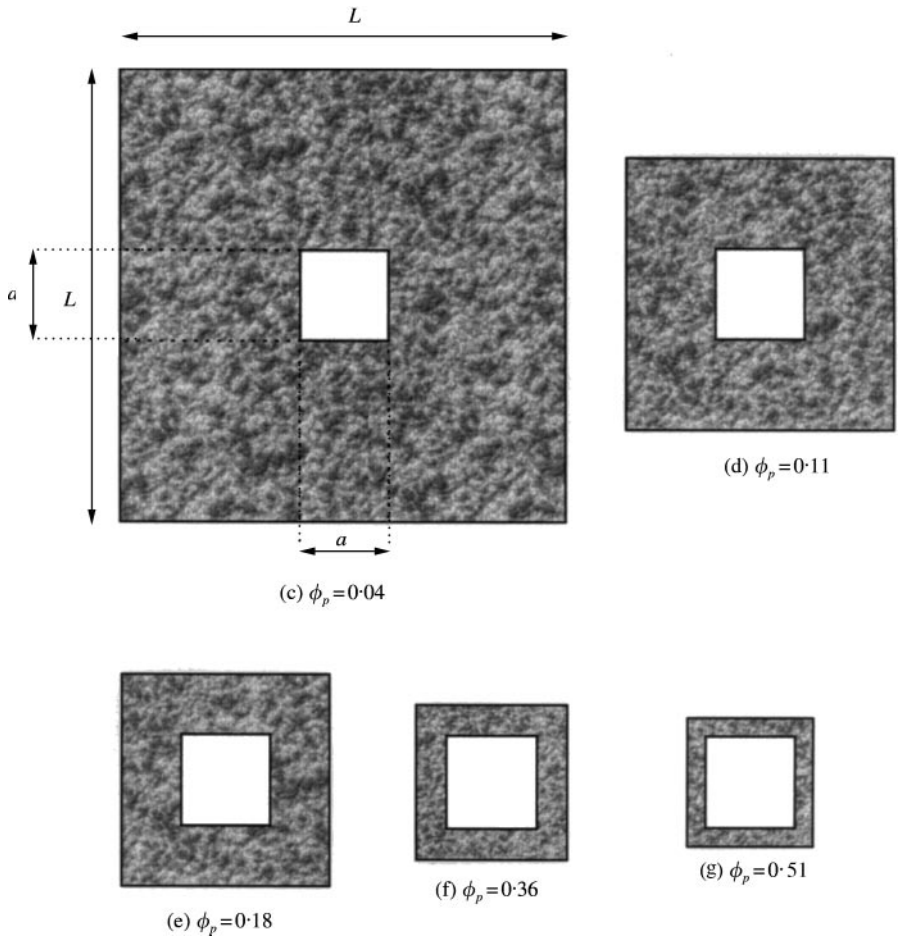

Figure 6. Configurations of interest

averaged surface impedance, not shown here, confirms this behavior. The imaginary part of the impedance equals zero at the first peak, attains a positive maximum at the drops of the absorption coefficient and passes through zero again at the second peak. When the hole size passes a certain limit, the maximum of the imaginary part of the impedance flattens and only one distinct broad absorption peak is observed. Finally, note that the absorption coefficient remains larger than that of the homogeneous material for all hole sizes. In consequence, the hole size may be used to control the bandwidth of the absorption peak.

4.3. INFLUENCE OF THE MACRO-PORES DISTRIBUTION

Figure 11 depicts one section of the configurations used to study the influence of the macro-pores distribution (in light grey in the figure). The macro-porosity is kept a constant equal to 0·18. The cell of interest is of size $L = 6{\cdot}6$ cm and is subdivided into seven different elementary cells which amounts to a hole size of 0·94 cm. Figure 12 present the effects on the absorption coefficient. It indicates that the largest absorption coefficient at low frequencies are obtained for cases (e) and (k), that is for a center square hole and a slot-like hole. However, cases (l), (m), (n) provide better results at higher frequencies, random case (l)

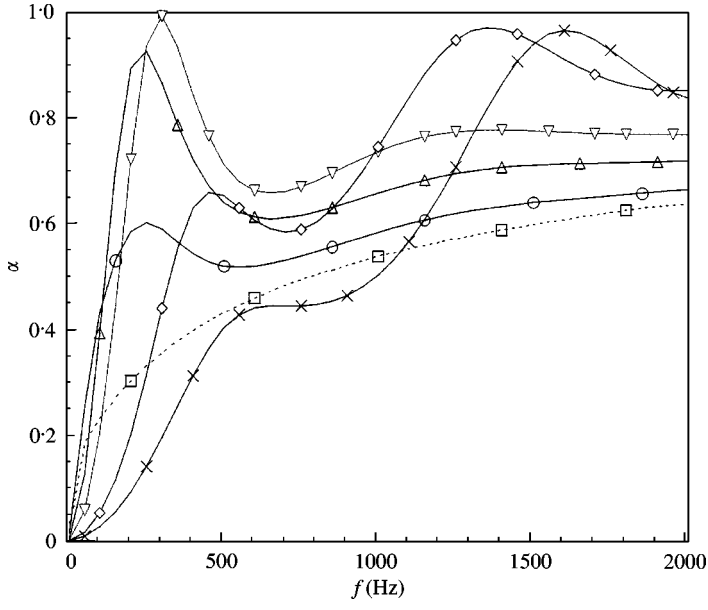

Figure 7. Effects of macro-porosity on the absorption coefficient: –□–, $\phi_p = 0$; —○—, $\phi_p = 0{\cdot}04$; —△—, $\phi_p = 0{\cdot}11$; —▽—, $\phi_p = 0{\cdot}18$; —◇—, $\phi_p = 0{\cdot}36$; —×—, $\phi_p = 0{\cdot}51$.

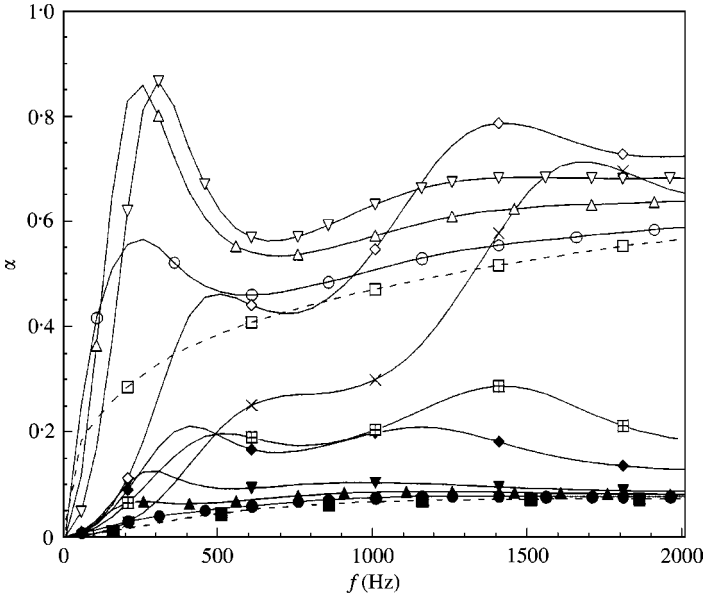

Figure 8. Effects of viscous and thermal dissipation mechanisms on the absorption coefficient for several macroporosities and $a = 2{\cdot}83$ cm. –□–, $\phi_p = 0$, Π_v; —■—, $\phi_p = 0$, Π_t; —○—, $\phi_p = 0{\cdot}04$, Π_v; —●—, $\phi_p = 0{\cdot}04$, Π_t; —△—, $\phi_p = 0{\cdot}11$, Π_v; —▲—, $\phi_p = 0{\cdot}11$, Π_t; —▽—, $\phi_p = 0{\cdot}18$, Π_v; —▼—, $\phi_p = 0{\cdot}18$, Π_t; —◇—, $\phi_p = 0{\cdot}36$, Π_v; —◆—, $\phi_p = 0{\cdot}36$, Π_t; —×—, $\phi_p = 0{\cdot}51$, Π_v; —■—, $\phi_p = 0{\cdot}51$, Π_t.

yielding intermediate performance between cases (m) and (n). In cases (e) and (k), the shape factor is about the same but the characteristic length Λ_d is higher than in cases (l), (m), (n) and therefore ω_d is smaller. A smaller diffusion frequency induces a larger bandwidth of the

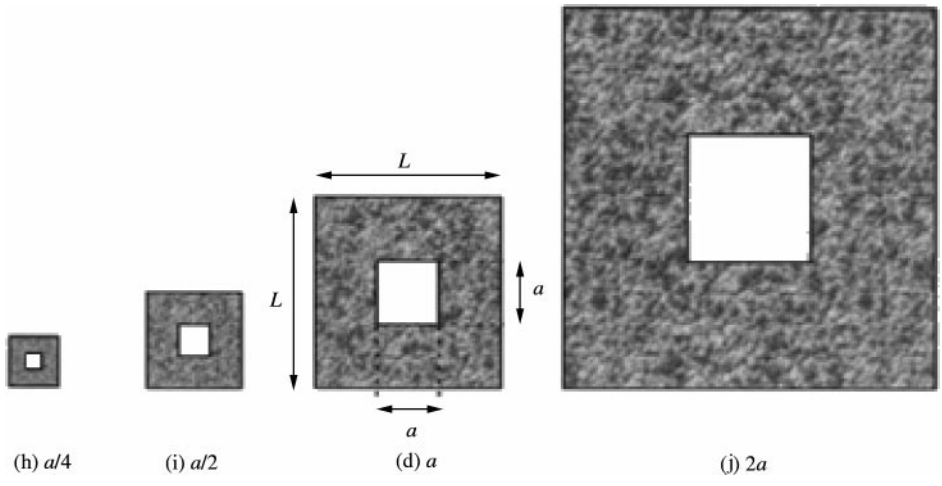

Figure 9. Configurations of interest.

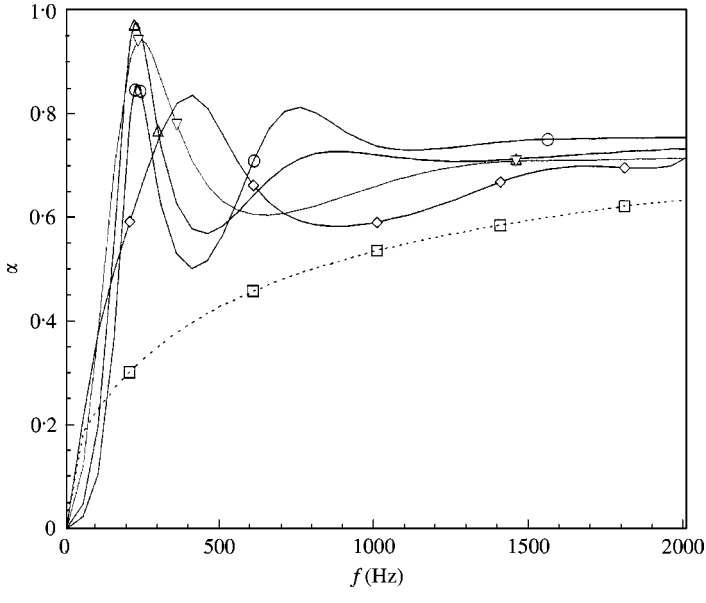

Figure 10. Effects of the hole size on the absorption coefficient ($\phi_p = 0{\cdot}11$). –□–, $\phi_p = 0$; —○—, $a/4$; —△—, $a/2$; —▽—, a; —◇—, $2a$.

absorption peak at low frequencies as pointed out by Olny [12]. This can be noticed in Figure 12.

4.4. INFLUENCE OF THE DOUBLE-POROSITY MATERIAL FLOW RESISTIVITY

In this section, the effect on the absorption coefficient of the flow resistivity of the micro-porous material constituting the double-porosity material of the previous sections ($\phi_p = 0{\cdot}11$; $h = 11{\cdot}5$ cm) is investigated. To keep the resulting materials realistic, the viscous and thermal characteristic length are varied as well in order to keep the viscous and thermal

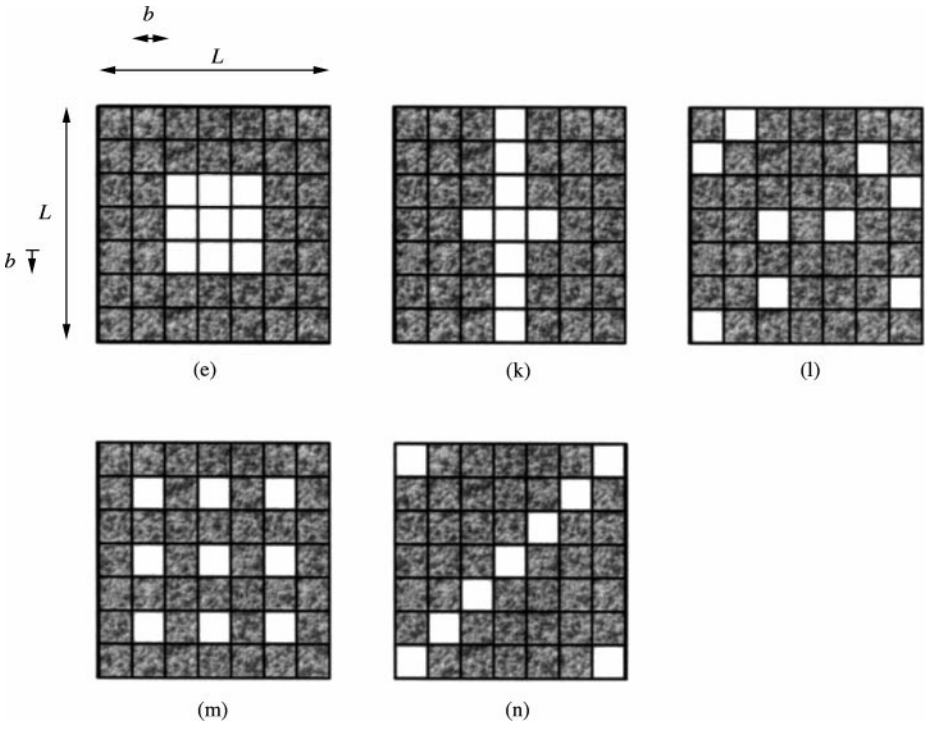

Figure 11. Configurations of interest.

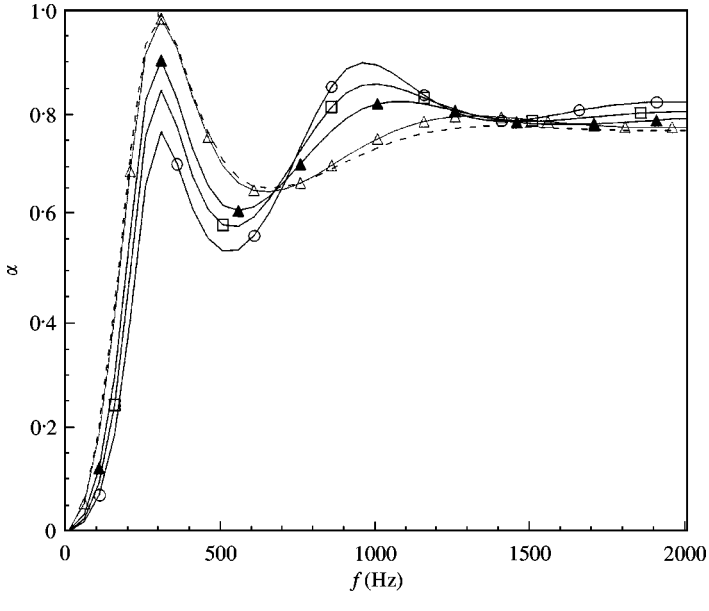

Figure 12. Effects of the macro-pores distribution on the absorption coefficient ($\phi_p = 0{\cdot}18$). – – –, case (e); –□–, case (k); –○–, case (l); –△–, case (m); –▲–, case (n).

shape factors constant. The other parameters remain unchanged. Figure 13 shows the influence of the flow resistivity on the absorption coefficient. Five flow resistivities are compared ($\sigma_0 = 135\,\mathrm{kN\,m^{-4}\,s}$; $\sigma_1 = 80\,\mathrm{kN\,m^{-4}\,s}$; $\sigma_2 = 40\,\mathrm{kN\,m^{-4}\,s}$; $\sigma_3 = 20\,\mathrm{kN\,m^{-4}\,s}$;

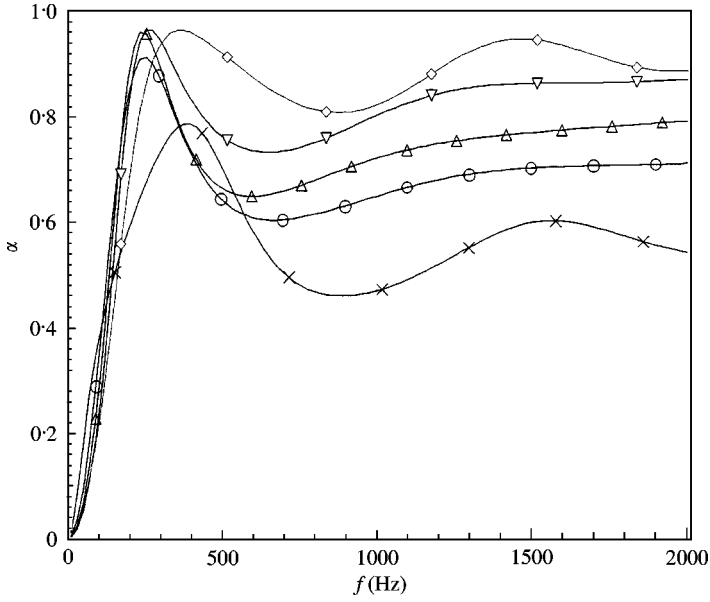

Figure 13. Influence of the flow resistivity of the microporous material on the absorption coefficient ($\phi_p = 0{\cdot}11$). —○—, σ_0; —△—, σ_1; —▽—, σ_2; —◇—, σ_3; —×—, σ_4.

$\sigma_4 = 400\ \mathrm{kN\,m^{-4}\,s}$). The main effect is that the frequency position of the peak increases with decreasing values of σ. Also it seems that the peaks becomes wider. As expected at higher frequencies best results are found for small values of σ. However, compared to the homogeneous cases, the best improvement is obtained in the case of large σ as seen in Figure 14. In consequence, macro-perforations work better for materials with a large flow resistance.

4.5. MACRO-PORES FILLED WITH A POROUS MATERIAL

In this paragraph, the effect of the flow resistivity of material inserted in the hole on the absorption performance of the system is investigated. A rigid glass wool (see Table 1 for measured properties) is used to fill the central hole of the 11·5 cm thick rock-wool elementary cell depicted in Figure 2, instead of air. The macro-porosity (defined here as the volume of the hole to the total volume) is kept constant to 0·11. Figure 15 shows the results for several flow resistivities (for each flow resistivity, the characteristic lengths are calculated in order to keep the shape factors constant). It is seen that in all cases, there is an improvement compared to the homogeneous configuration. The best results are obtained for cases with the largest contrast between the flow resistivities of the two constitutive materials. The larger the contrast, the lower the frequency position of the absorption peak. However, using a moderate flow resistivity allows for a much wider peak and an improved performance over the entire frequency range.

4.6. ABSORPTION OF A NON-HOMOGENEOUS POROUS MATERIAL

Finally, a multi-layered material made up from a 5 cm thick layer of the rock-wool used in the previous sections and a 1 cm thick layer of a low resistivity rigid glass wool (RGW)

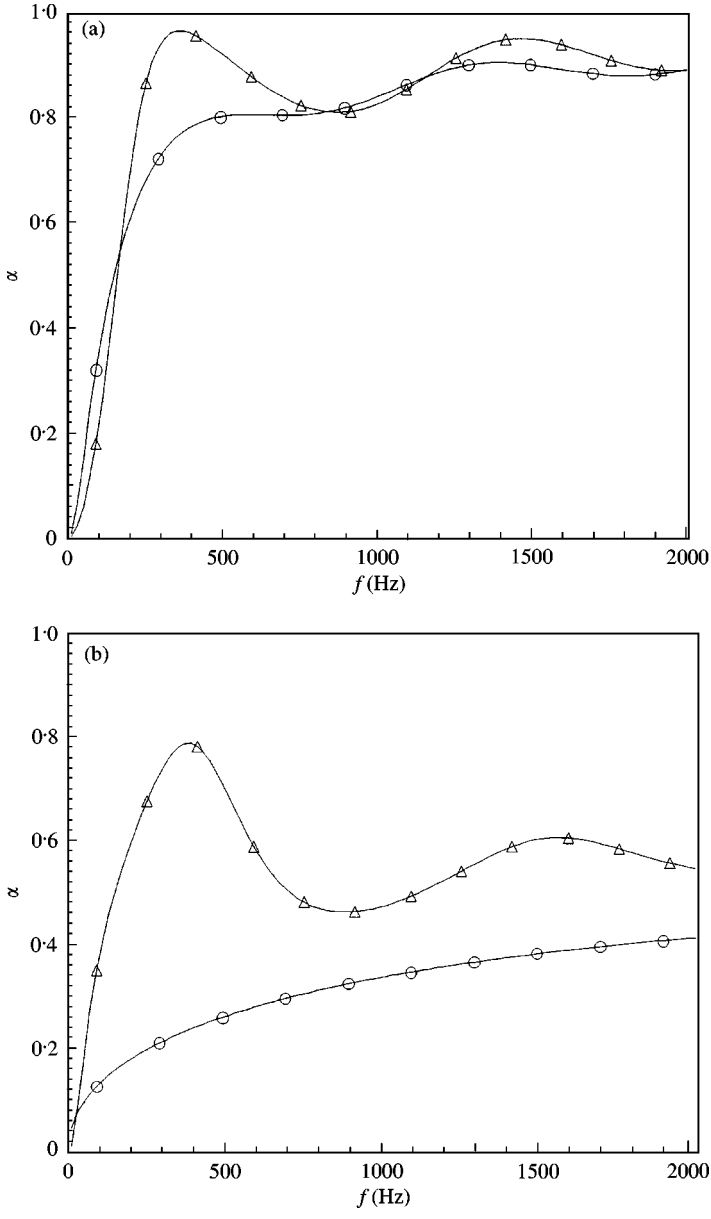

Figure 14. Influence of the flow resistivity of the microporous material on the absorption coefficient. Comparison between the homogeneous and the double-porosity material ($\phi_p = 0{\cdot}11$) for: (a) $\sigma_3 = 20\,\mathrm{kN\,m^{-4}\,s}$; (b) $\sigma_4 = 400\,\mathrm{kN\,m^{-4}\,s}$. —○—, $\phi_p = 0$; —△—, $\phi_p = 0{\cdot}11$.

(see Table 1 for properties) are considered. The rock-wool layer is bonded onto the hard-walled termination of the waveguide. Figure 16, compares the sound absorption of the multi-layer to a non-homogeneous configuration in which the RGW is randomly distributed within the material while keeping the ratio of the volume occupied by the two materials constant. It is shown that a better absorption coefficient is attained in the non-homogeneous case. This result confirms that the different patches do interact and a better sound absorption can be achieved using the non-homogeneous configuration.

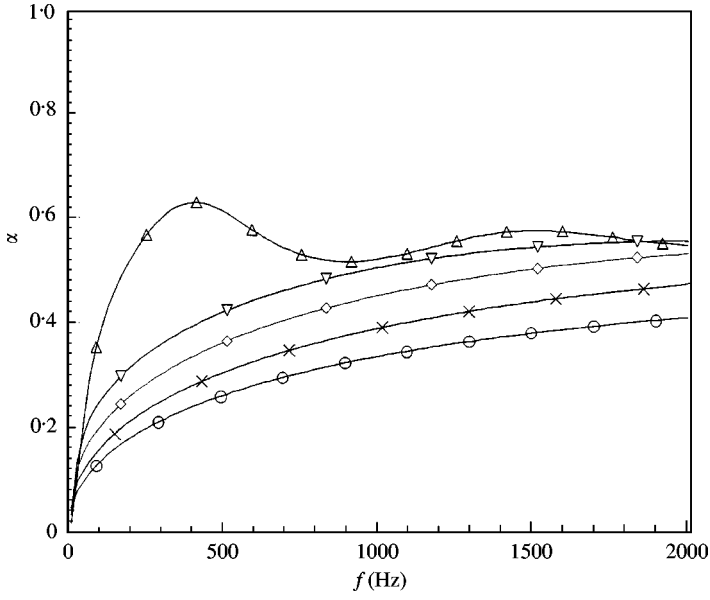

Figure 15. Effects of the flow resistivity contrast on the absorption coefficient for holes filled with a porous material. —○—, $\phi_p = 0$; —△—, $\sigma_p = 2000$; —▽—, $\sigma_p = 15000$; —◇—, $\sigma_p = 30000$; —×—, $\sigma_p = 80000$.

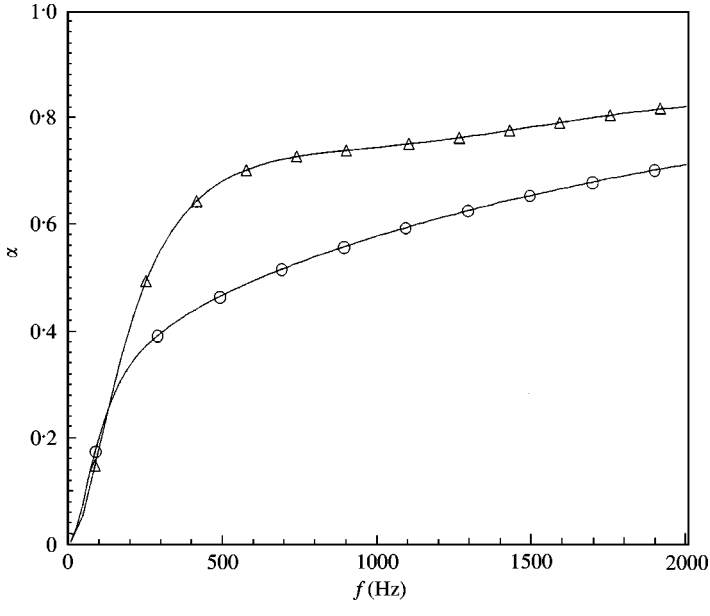

Figure 16. Comparison of a two-layers material to an equivalent non-homogeneous material: —○—, two-layers; —△—, double porosity.

5. CONCLUSION

The absorption coefficient of non-homogeneous porous layers has been predicted from a 3-D numerical finite element model where each patch is modelled as an equivalent fluid.

An experimental validation has been presented and proved the accuracy of the presented model. Based on a numerical parameter study, it is shown that surrounding patches interact together and better performances are obtained for non-homogeneous materials than for homogeneous simple layered materials. In particular, it has been shown that properly designed macro-perforated porous materials allow for an important increase of the absorption performances at low frequencies without any loss at higher frequencies.

ACKNOWLEDGMENTS

This work has been made possible with the combined financial support of NSERC (National Sciences and Engineering Research Council of Canada) and IRSST (Institut de Recherche en Santé et Sécurité au Travail, Quebec).

REFERENCES

1. J. ALLARD 1993 *Propagation of Sound in Porous Media, Modelling Sound Absorbing Materials.* New York and London: Elsevier Application Science, 284p.
2. B. BROUARD, D. LAFARGE and J. ALLARD 1995 *Journal of Sound and Vibration* **183**, 129–142. General method of modeling sound propagation in layered media.
3. U. INGARD 1994 *Notes on Sound Absorption Technology* version 94-02, New York, USA: Noise Control Foundation, 347pp.
4. A. BARDOT, B. BROUARD and J. ALLARD 1996 *Journal of Applied Physics* **79**, 8223–8229. Frame decoupling at low frequencies in thin porous layers saturated by air.
5. N. ATALLA, R. PANNETON and P. DEBERGUE 1998 *Journal of the Acoustical Society of America* **104**, 1444–1452. A mixed displacement-pressure formulation for poroelastic materials.
6. Y. KANG anmd J. BOLTON 1995 *Journal of the Acoustical Society of America* **98**, 635–643. Finite element modeling of isotropic elastic porous materials coupled with acoustical finite elements.
7. R. PANNETON and N. ATALLA 1997 *Journal of the Acoustical Society of America* **101**, 3287–3298. An efficient finite element scheme for solving the three-dimensional poroelasticity problem in acoustics.
8. N. ATALLA, R. PANNETON and J. ALLARD 1996 *Acta Acustica* **93**, 891–896. Sound absorption by non homogeneous thin porous layers.
9. J. AURIAULT and C. BOUTIN 1994 *Transport in Porous Media* **14**, 143–162. Deformable porous media with double porosity III: Acoustics.
10. C. BOUTIN and X. OLNY 1999 *Mécanique des Matériaux Hétérogènes* Grenoble, France, 29–34. Mécanique des matériaux hétérogènes.
11. C. BOUTIN, P. ROYER and J. AURIAULT 1998 *International Journal of Solids Structures* **35**, 4709–4737. Acoustic absorption of porous surfacing with dual porosity.
12. X. OLNY 1999 *Ph.D. Thesis, Institut National des Sciences Appliquées de Lyon.* Absorption acoustique des milieux poreux à simple et double porosité-Modélisation et validation expérimentale. 262p.

APPENDIX A: NOMENCLATURE

$\mathbf{g}$	a vector
$\boldsymbol{g}$	a tensor
∇	Nabla operator
∇g	gradient of $\mathbf{g}$
$\nabla \cdot \mathbf{g}$	divergence of $\mathbf{g}$
$\mathbf{g}^*$	complex conjugate of $\mathbf{g}$
L_1, L_2	lateral dimensions of the waveguide
$\mathbf{x} = (x_1, x_2, x_3)$	vector locating a point in space
ρ_0	density of the fluid in the waveguide

c_0	sound speed of the fluid in the waveguide
ω	circular frequency
ϕ	porosity
$\tilde{\rho}_{22}$	effective fluid density of the porous media
$\tilde{R}$	effective bulk modulus of the porous media
p	pressure in the equivalent fluid
Ω^p	volume of the porous material
$\partial\Omega^p$	bounding surface enclosing Ω^p
$\mathbf{n}$	unit normal vector external to $\partial\Omega^p$
$\partial/\partial n$	normal derivative
δp	arbitrary admissible variation of p
p^a	acoustic pressure in the waveguide
u_n^a	normal particular displacement associated to p^a
p_b	blocked pressure
p_{rad}	pressure radiated in the waveguide by the surface of the patch-work media
p_0	amplitude of the excitation mode
B_{mn}, C_{mn}	modal amplitudes of mode (m, n) for variable p_{rad} and p respectively
$\varphi_{mn}(x_1, x_2)$	mode (m, n) of the waveguide; for a rectangular cross-section $\varphi_{mn}(x_1, x_2) = \cos((\pi m/L_1)x_1)\cos((\pi n/L_2)x_2)$
k_{mn}	tangential wave number of mode (m, n); $k_{mn}^2 = k^2 - (m\pi/L_1)^2 - (n\pi/L_2)^2$
$k = \omega/c_0$	wave number in the waveguide
$S = L_1 \times L_2$	area of the waveguide cross-section
N_{mn}	norm of mode (m, n)
$\boldsymbol{A}(\mathbf{x}, \mathbf{y})$	admittance operator
Π_{int}	power developed by the internal forces in the interstitial fluid
Π_{iner}	power developed by the inertia forces in the interstitial fluid
Π_{trans}	power flowing into the waveguide-porous interface
Π_{diss}	time-averaged power dissipated within the system
Π_{diss}^v	time-averaged power dissipated through viscous effects in the porous material
Π_{diss}^t	time-averaged power dissipated through thermal effects in the porous material
Π_{inc}	time-averaged incident power
α	absorption coefficient
Π_{ref}	time-averaged reflected power
p_{avg}	surface-averaged pressure
Z_d	space-averaged surface impedance at distance d from the material
Z_s	surface impedance
$Z_0 = \rho_0 c_0$	characteristic impedance of the fluid in the waveguide
d	distance from the material surface
L_c	lateral dimension of a generic cell
a	size of the hole
ϕ_m	porosity of the porous material
ϕ_p	porosity associated to the holes
h	thickness of the macro-perforated material
ω_d	diffusion circular frequency for a double-porosity material
σ_m	flow resistivity of the porous material
D_{eq}	function depending on the geometry of the hole lattices
$P_0 = 101\,300$ Pa	ambient pressure
M_d	shape factor depending on the hole shapes and on the macro-pores distribution
Λ_d	characteristic length associated with the diffusion process